Front. Mater. Sci. 2018, 12(4): 415–425
https://doi.org/10.1007/s11706-018-0442-z

RESEARCH ARTICLE

Synthesis of sillenite-type $Bi_{36}Fe_2O_{57}$ and elemental bismuth with visible-light photocatalytic activity for water treatment

Chuan DENG[1,2], Xianxian WEI (✉)[1], Ruixiang LIU[2], Yajie DU[1], Lei PAN[1], Xiang ZHONG[1], and Jianhua SONG[1]

1 College of Environment and Safety, Taiyuan University of Science and Technology, Taiyuan 030024, China
2 College of Environmental Science and Engineering, Taiyuan University of Technology, Taiyuan 030024, China

ABSTRACT: With $Fe(NO_3)_3 \cdot 9H_2O$ and $Bi(NO_3)_3 \cdot 5H_2O$ as raw materials, different sillenite-type compounds and elemental bismuth were prepared by a facile one-pot solvothermal method using H_2O, C_2H_5OH, $(CH_2OH)_2$ and $C_3H_8O_3$ as solvents, respectively. The structure, morphology, elemental compositions and properties of samples were examined by XRD, SEM, TEM, ICP, XPS, N_2 adsorption and desorption, UV-vis DRS and PL. The photocatalytic activities of different samples were evaluated by the photodegradation of RhB under visible-light irradiation ($\lambda > 400$ nm), and results show that $Bi_{36}Fe_2O_{57}$ prepared using C_2H_5OH as the solvent owns the optimum performance. In order to explore the reaction mechanism, an additional experiment was designed to investigate the main active species during the photodegradation process via dissolving different trapping agents in the reaction solution before light irradiation. The results show that superoxide radical anions play a major role in this system since the RhB degradation was significantly suppressed after the addition of benzoquinone.

KEYWORDS: photocatalysis; sillenite; elemental Bi; $Bi_{36}Fe_2O_{57}$

Contents

Received July 13, 2018; accepted September 27, 2018

E-mail: weixianxian@tyust.edu.cn

1 Introduction

In recent years, water pollution has become an important part of environmental pollution, and among which dye wastewater not only poses a threat to the environment but also seriously endangers human health [1–2]. According to a statistical report (UNICEF and FAO Joint Report), it is estimated that there are 780 million people who are difficult

to get clean drinking water, most of which coming from developing countries in the world. As a big developing country for textile production and processing, China's annual dye production reaches 1.5×10^5 t, about 10%–20% of which included in wastewater discharged directly into the body of water, causing serious pollution [3]. In order to protect the environment from contamination caused by dye wastewater and to reduce the threat to human health caused by water-borne diseases, it is necessary to study a greener and more sustainable method to effectively control the water pollution. At present, photocatalysis, as one of the most promising technologies with its advantages of low-energy consumption, simple operation, mild reaction conditions and no secondary pollution [4–8], has been widely concerned about.

The traditional photocatalytic materials are mainly TiO_2 semiconductor oxides [9]. In recent years, scientists have explored new types of photocatalytic materials in two directions. One is based on the modification of compositions of TiO_2, and the other is dedicated to the discovery of other classes of photocatalytic materials which include elemental metals, elemental non-metals, compound-type semiconductor oxides, and composite photocatalytic materials. Elemental materials which can be used as photocatalytic materials always have rich sources and can be obtained in nature. Therefore, the research on single photocatalytic materials has been gradually increased in recent years. It has been found that non-metallic elements, e.g., B, P and S, have photocatalytic properties [10–12]. In addition, the application of metal elements in the field of photocatalysis has also begun to receive attention. For instance, bismuth-based materials are well known for their good photocatalytic activity, and some scholars have carried out research on elemental bismuth. Qin et al. [13] synthesized uniform bismuth nanospheres by the hydrothermal method, which were used for photodegrading potassium dichromate, and the results showed that elemental bismuth has excellent visible-light photocatalytic performance that Cr(VI) could be reduced to less toxic lower-valent Cr(III). Ma et al. [14] synthesized one-dimensional (1D) bismuth nanostructures at low temperature, and performance testing showed that the visible-light degradation of rhodamine B (RhB) under acidic conditions was objective, but the photocatalytic performance under neutral conditions was very weak. Wang et al. [15] synthesized pure-phase elemental bismuth by thermolysis of bismuth acetate in oleylamine, and the characterization showed that there were three absorption peaks in the UV-visible region. Cui et al. [16] obtained pure-phase bismuth nanoparticles with an average size of 70 nm by the microwave method and observed an apparent absorption edge at 700 nm, based on which the authors believed that the bismuth was undergoing a transition from a semimetal to an indirect semiconductor.

Researchers are devoted to working on photocatalytic properties of elemental bismuth and other bismuth-based compounds, a very important group of which are compounds with the sillenite structure [17] regarded as visible-light driven photocatalysts. The general formula of sillenite-type compounds is $Bi_{12}MO_{20\pm\delta}$ (M = Ni, Al, Ti, Fe, etc.) with the space group of I23 and no symcenter. $Bi_{12}MO_{20\pm\delta}$ is one of the most promising catalysts and has attracted attention of many researchers due to its unique optical and electrical properties [18–21], exhibiting a multitude of application prospects in a couple of fields such as photoconduction and visible-light photocatalysis. Zhang et al. [19] used the hydrothermal method to prepare a sillenite-type crystal $Bi_{25}FeO_{40}$ and evaluated its photocatalytic performance by the degradation of methyl violet solution under UV-vis light irradiation. It was found that $Bi_{25}FeO_{40}$ is efficient for photodegradation due to its special crystal structure. Li et al. [22] synthesized $BiFeO_3$, $Bi_2Fe_4O_9$ and $Bi_{25}FeO_{40}$ powders by adjusting the concentration of NaOH. Hang et al. [23] reported a sillenite-type crystal $Bi_{12}Fe_{0.63}O_{18.945}$ synthesized by the microwave hydrothermal method and demonstrated that this sillenite-type bismuth ferritic nanocrystal is a promising visible-light-responsive photocatalyst for the degradation of organic compounds. However, at present, there are still few studies on sillenite-type materials, and the research on the emerging photocatalyst $Bi_{36}Fe_2O_{57}$ is even rarer.

In this work, pure-phase $Bi_{36}Fe_2O_{57}$ and elemental bismuth were successfully prepared by a simple solvothermal method using H_2O, C_2H_5OH, $(CH_2OH)_2$ and $C_3H_8O_3$ as solvents, respectively. The influence of the initial solvent on physicochemical properties of such photocatalysts was discussed, especially for the influence of solvents on the structural evolution of prepared materials, in which $Fe(NO_3)_3\cdot9H_2O$ and $Bi(NO_3)_3\cdot5H_2O$ were used as raw materials. The photocatalytic performance was evaluated by visible-light degradation of RhB, and the photocatalytic reaction mechanism of $Bi_{36}Fe_2O_{57}$ was also systematically investigated.

2 Experimental

2.1 Sample preparation

Reagents used in the experiment were of analytical grade. The typical experimental process is as follows: Firstly, 808 mg $Fe(NO_3)_3 \cdot 9H_2O$ and 485 mg $Bi(NO_3)_3 \cdot 5H_2O$ were dissolved in 20 mL of 1 mol/L HNO_3 solution, and 40 mL of 1 mol/L NaOH solution was added dropwise after the magnetic stirring for 30 min. Four identical mixtures were prepared as described above. Then 20 mL of 1 mol/L NaOH solution, ethanol, ethylene glycol and glycerol were respectively added into the above four mixtures with the magnetic stirring for 30 min. The above solutions were transferred into 100 mL PTEE-lined stainless steel autoclaves and the reactors were placed in a homogeneous reactor at 150°C for 12 h. Centrifuge the samples thoroughly with deionized water and absolute ethanol, and repeat until the pH of the supernatant after centrifugation was approximately 7. Drying in an oven at 50°C to constant weight to obtain pure-phase materials, and the samples were labeled as $Bi_{36}Fe_2O_{57}$–H_2O (BFO), $Bi_{36}Fe_2O_{57}$–C_2H_5OH (BFO–C_2H_5OH), Bi–$(CH_2OH)_2$ and Bi–$C_3H_8O_3$, respectively.

2.2 Characterization

Crystal structures of the samples were characterized by X-ray diffraction (XRD) on a D8 ADVANCE with Cu Kα radiation ($\lambda = 0.154$ nm), tube current of 100 mA and tube voltage of 40 kV. The surface chemical composition study was carried out using X-ray photoelectron spectroscopy (XPS, Thermo Scientific ESCALAB 250Xi). The total (bulk) Bi and Fe contents were determined by an inductive coupled plasma (ICP) emission spectrometer (Agilent ICP OES 730). The morphology of the sample was characterized by field-emission scanning electron microscopy (FESEM, JSM-7001F). In order to observe the microscopic morphology and crystallographic properties ofthe samples, transmission electron microscopy (TEM), high-resolution transmission electron microscopy (HRTEM) and selected area electron diffraction (SAED) studies were performed on a JEOL (JEM-2100F) microscope. In addition, the N_2 adsorption and desorption isotherms were measured on a Tristar 3000 sorptometer at 77 K with the samples degassed for 12 h at 80°C under vacuum. The characteristic surface area (S_{BET}) and the pore size distribution of the material were estimated using the Brunauer–Emmertt–Teller (BET) method and the Barret–Joyner–Halenda (BJH) method, respectively. Diffuse reflectance UV-vis absorbance spectroscopy (DRS) results were recorded by using a Shimadzu UV-2550 spectrophotometer equipped with an integrated sphere and using $BaSO_4$ as the reference. The photoluminescence (PL) spectrum was measured on a Hitachi F-7000 fluorescence spectrophotometer with the 260 nm excitation wavelength.

2.3 Photocatalytic activity test

The photocatalytic degradation of RhB was employed to evaluate photocatalytic activities of the samples under visible-light irradiation of a 300 W Xe lamp with a 400 nm cut-off filter. 25 mg catalyst was suspended in 100 mL RhB solution (10 mg/L). Before irradiation, the suspensions were magnetically stirred for 30 min in the dark to ensure the adsorption–desorption equilibrium. Then the suspensions were exposed to visible-light illumination. The time is 60 min and the interval is 10 min. In addition, 3 mL of RhB solution without catalyst and 3 mL of solution after magnetic stirring were taken as the blank and the contrast samples, respectively. In the degradation process, magnetic stirring should always be maintained to avoid the agglomeration of catalyst particles [24]. Meanwhile, in order to prevent the thermal catalysis from the irradiation of light source [25], circulating cooling water should be provided in the entire degradation process to ensure the system temperature at room temperature. The supernatant after centrifuging was taken out for the UV-vis absorption spectrum measurement at 554 nm. The degradation rate (η) of the photocatalytically degraded RhB is given by Eq. (1) as follow:

$$\eta = c/c_0 \tag{1}$$

where c_0 is the initial concentration of RhB and c is the concentration of RhB after light irradiation.

2.4 Discussion of photocatalytic mechanism

In order to study the photocatalytic reaction mechanism, another experiment was designed to detect the major active groups in the photocatalytic reaction [17,26–27]. Different capture agents, benzoquinone (BQ), ammonium oxalate (AO), silver nitrate ($AgNO_3$) and tert-butyl alcohol (TBA), were added into the reaction system to capture superoxide radicals ($\bullet O_2^-$), photo-induced holes (h^+), electrons (e^-) and hydroxyl radicals (•OH), respectively. The amount of the capturing agent was 0.5 mmol, and the photocatalytic performance after the addition of the capturing agent was evaluated as described above.

3 Results and discussion

3.1 Structure and morphology characterization

3.1.1 XRD

Crystal structures of the samples were examined by XRD measurements (Fig. 1). As shown in Fig. 1(a), the diffraction peak positions of BFO and BFO–C_2H_5OH are similar, though peaks of BFO are weaker than those of BFO–C_2H_5OH. No other impurity peak appears, and the diffraction peaks at 2θ = 24.7°, 27.7°, 32.9°, 41.6°, 52.3°, 55.6°, 61.7° and 78.5° correspond to the planes of (220), (310), (321), (332), (530), (532), (631) and (653), respectively, indexed to the pure cubic phase of $Bi_{36}Fe_2O_{57}$ (JCPDS No. 42-0181) [18]. As the diffraction line with an odd number of $(h + k + l)$ does not appear, it is inferred that such two samples belong to the body-centered cubic (bcc) phase [28]. Therefore, it is clear that using either deionized water or ethanol as the solvent, a pure-phase sample $Bi_{36}Fe_2O_{57}$ can be synthesized, and $Bi_{36}Fe_2O_{57}$ synthesized using the ethanol solvent has better crystallinity. As shown in Fig. 1(b), the diffraction peak positions of Bi–$(CH_2OH)_2$ and Bi–$C_3H_8O_3$ are similar, while peaks of Bi–$(CH_2OH)_2$ are stronger than those of Bi–$C_3H_8O_3$. The diffraction peaks at 2θ = 27.2°, 37.9°, 39.6°, 48.7°, 56.1°, 62.2°, 64.5° and 71.5° correspond to the planes of (012), (104), (110), (202), (024), (116), (122) and (009), respectively, indexed to elemental bismuth with the prism structure (JCPDS No. 05-0519) [29], indicating that elemental bismuth can be synthesized using either ethylene glycol or glycerol as the solvent, and ethylene glycol leads to better crystallinity compared with glycerol.

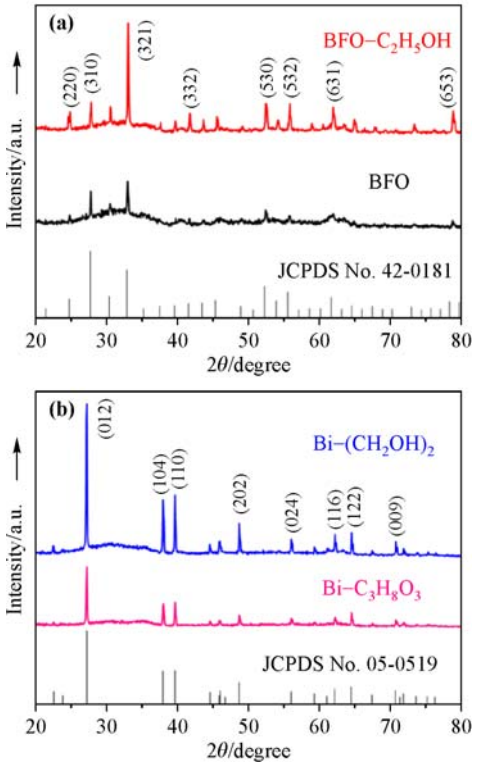

Fig. 1 XRD patterns: **(a)** BFO and BFO–C_2H_5OH; **(b)** Bi–$(CH_2OH)_2$ and Bi–$C_3H_8O_3$.

3.1.2 XPS and ICP

XPS measurements were performed to check the type and the valence of each element of BFO–C_2H_5OH. From Fig. 2 (a) it is seen that there are Bi, O and Fe peaks, which confirm chemical compositions of the sample, while the peak at 284.5 eV corresponds to the standard peak of carbon. A narrow range scan was performed to detect each element in the sample, and Figs. 2(b), 2(c) and 2(d) show high resolution spectra of Bi 4f, Fe 2p and O 1s, respectively. Two basic symmetrical peaks located at 158.88 and 164.18 eV are revealed in Fig. 2(b), of which the former corresponds to the binding energy of Bi $4f_{7/2}$ and the latter to that of Bi $4f_{5/2}$, indicating that the bismuth element in the sample mainly exists in the form of Bi^{3+} [30–31]. As shown in Fig. 2(c), there are two strongest peaks at 710.78 and 724.18 eV, which are assigned to the Fe $2p_{3/2}$ and Fe $2p_{1/2}$ spin–orbit interaction, respectively [32]. Moreover, a satellite peak at 718.43 eV was found from the spectrum with the interval distance between the first two dotted lines of about 8 eV, and another satellite peak at 733.08 eV was also about 8 eV away from the main peak Fe $2p_{1/2}$. In principle, the satellite peak accompanied with the main peak appears due to the oxidation of Fe. Since Fe^{2+} and Fe^{3+} have different energies in the valence band, the position of the corresponding satellite peak is also different. In turn, the position of the satellite peak can reflect the oxidation state of the Fe element [33]. Because the chemical valence of Fe is very complicated, it is very difficult to analyze the Fe $2p_{3/2}$ photoelectron peak. Thus the chemical valence of Fe is often judged based on the satellite peak. The Fe^{2+} peak is always associated with a satellite peak at 6.0 eV above the principal peak, while the Fe^{3+} peak is associated with a satellite one at 8.0 eV above the principal one [34]. Combined with the XPS spectrum in Fig. 2(c), it can be concluded that the element Fe in the sample exists in the trivalent state. Figure 2(d) shows the high-resolution spectrum of O 1s. The main peak is located at 529.74 eV, which can be divided into two sub-bands at

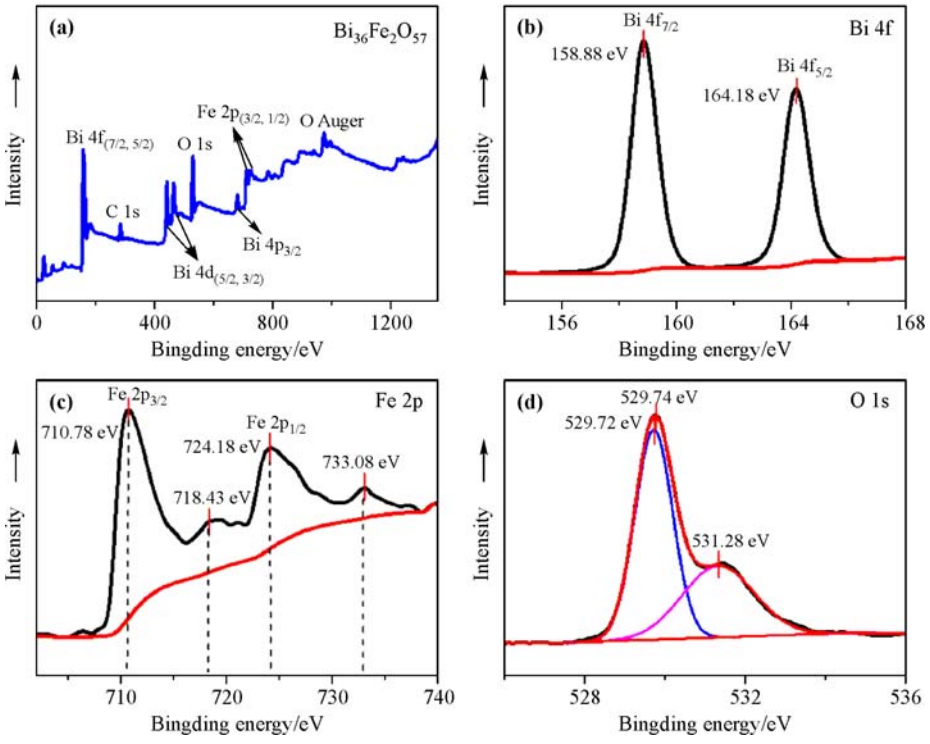

Fig. 2 XPS results: **(a)** full spectrum of BFO–C_2H_5OH; **(b)(c)(d)** high-resolution spectra of Bi, Fe and O elements.

529.72 and 531.28 eV corresponding to the O 1s binding energies of BFO–C_2H_5OH and the impurity phase in the sample, respectively [35].

Also, the surface and the bulk elemental compositions were analyzed by XPS and ICP, respectively, and the results were summarized in Table 1. As are shown, the surface molar ratio n(Bi)/n(Fe) was calculated to be 0.67 from the XPS analysis, which is close to that of the bulk composition from ICP (0.52). According to the experimental section, the raw material molar ratio n(Bi)/n(Fe) was 0.5, which is in accordance with the results of XPS and ICP. However, the crystal structure of the BFO–C_2H_5OH sample was pure cubic phase of $Bi_{36}Fe_2O_{57}$ by XRD and TEM, in which the molar ratio n(Bi)/n(Fe) is 18. This could be owing to that most irons exist as the amorphous form.

3.1.3 SEM and TEM

Typical SEM images of BFO, BFO–C_2H_5OH, Bi–$(CH_2OH)_2$ and Bi–$C_3H_8O_3$ are shown in Fig. 3. As can be seen, all images show irregular block structure. This may be due to the strong hydrolysis of $Bi(NO_3)_3 \cdot 5H_2O$ in aqueous solution to form water-insoluble bismuth subnitrate or bismuth nitrate [36–37] during the catalyst preparation by the solvothermal method, making it difficult to obtain morphology-controlled and stoichiometric products [38]. Moreover, due to the addition of the NaOH solution and other alcoholic solvents, the pH value of this system changes. The larger the concentration of OH^- in the system is, the higher the supersaturations of Bi^{3+} and Fe^{3+} are, and the faster the precipitated grains are generated with less likelihood to form the crystalline in regular geometric shape [18]. It can also be seen from Figs. 3(a) and 3(b) that some fine particles get attached to large ones, indicating that the growth of BFO follows the Ostwald maturation mechanism [39], whereas in Figs. 3(c) and 3(d), the agglomeration phenomenon indicates that the growth of elemental bismuth follows the growth mechanism of nucleation and agglomeration [40]. In general, reaction conditions have a large influence on morphology, particle

Table 1 Surface and bulk elemental compositions of BFO–C_2H_5OH resulting from XPS and ICP analyses

Method	Surface elemental compositions		Bulk elemental compositions		Molar ratio of n(Bi)/n(Fe)
	c(Bi)/at.%	c(Fe)/at.%	w(Bi)/mass%	w(Fe)/mass%	
XPS	8.43	12.53	–	–	0.67
ICP	–	–	59.13	30.43	0.52

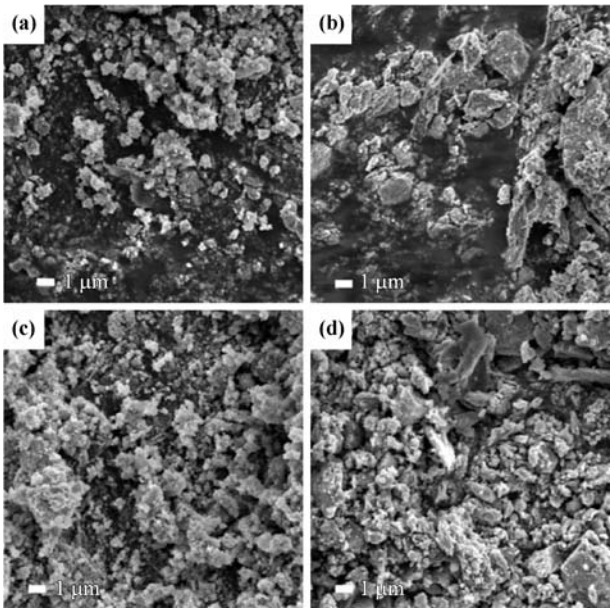

Fig. 3 SEM images of **(a)** BFO, **(b)** BFO–C_2H_5OH, **(c)** Bi–$(CH_2OH)_2$ and **(d)** Bi–$C_3H_8O_3$.

size and electrical conductivity of the sample [41]. However, there is no significant difference in the morphology of all samples, which may be related to the same preparation conditions, the same kind and concentration of precursor solutions and mineralizers. Furthermore, the size distribution of the irregular block sample is narrow, about 1–3 μm from the SEM observation, while the crystallite size calculated by the XRD pattern using the Scherrer formula is dozens of nanometers. Therefore, TEM was applied to further observe the microscopic morphology and the crystalline structure.

The sample BFO–C_2H_5OH was selected to be further characterized by TEM and HRTEM. As shown in Fig. 4, BFO–C_2H_5OH is composed of both polycrystalline and single-crystalline. In Fig. 4(a), the sample BFO–C_2H_5OH exhibits micron-scale plate structure, which is assembled by dozens of nanometers particles. The SAED image indicates that these nanoparticles are polycrystallines and also confirms the formation of cubic $Bi_{36}Fe_2O_{57}$ by showing the diffraction rings of the (400) and (710) crystal planes (Fig. 4(a) inset). The corresponding HRTEM image reveals a lattice fringe with the spacing of 0.25 nm (Fig. 4 (b)), in accordance with the (400) plane of $Bi_{36}Fe_2O_{57}$. In Fig. 4(c), the TEM and SAED images reveal clear diffraction spots, indicating that the particles are single crystals identified by diffraction planes of (220) and (400) with the angle between them of about 45°, equal to the theoretical value. Furthermore, the lattice distances of ~0.25 and ~0.36 nm are in accordance with the planes (400) and (220), respectively (Fig. 4(d)), further verifying that the sample BFO–C_2H_5OH is cubic-phase $Bi_{36}Fe_2O_{57}$.

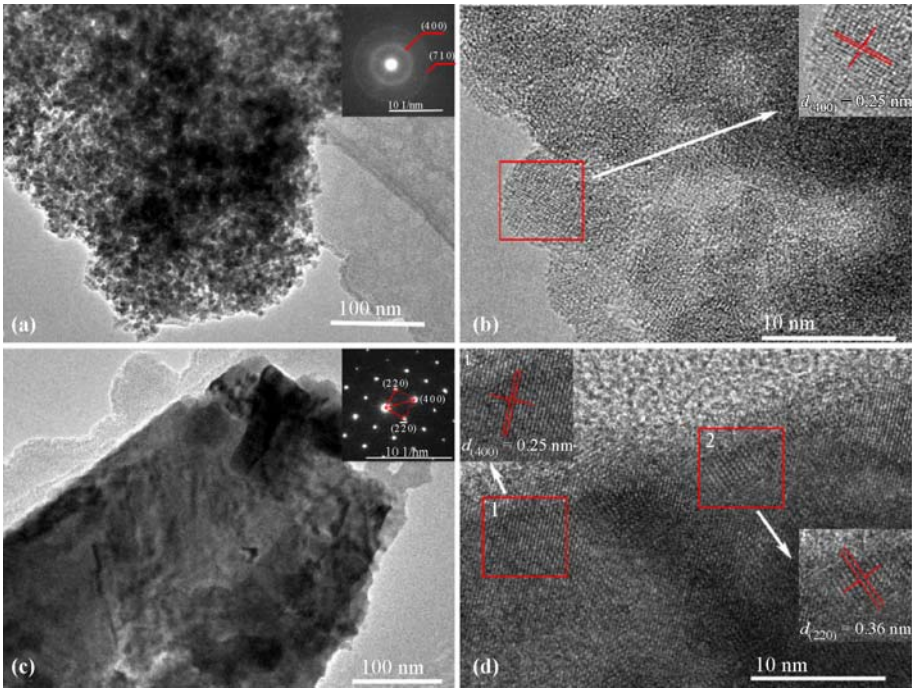

Fig. 4 Morphologies and structures of polycrystalline (upper) and single-crystalline (lower) in BFO–C_2H_5OH: **(a)(c)** TEM and SAED (inset) images; **(b)(d)** corresponding HRTEM images.

3.1.4 N_2 adsorption–desorption isotherms

Figure 5 presents N_2 adsorption–desorption isotherms and corresponding pore-size distribution (PSD) curves of four samples. According to the classification of Gibbs adsorption isotherms, all four samples show basic characteristics of type IV isotherms [42]. The adsorption–desorption curve is composed of inclined adsorption branches and steep desorption branches, and the two branches do not overlap to form a retention loop, resulting in a sudden emptying of the porous structure [42–43]. The formation of hysteresis loop is related to the capillary condensation phenomenon, and adsorption occurs when the relative pressure p/p_0 increases to a certain degree [42,44]. BFO–C_2H_5OH and Bi–$C_3H_8O_3$ belong to the H2 type hysteresis loop, while BFO and Bi–$(CH_2OH)_2$ belong to the H1 type. The p/p_0 values of BFO–C_2H_5OH and Bi–$(CH_2OH)_2$ are in the range from 0.4 to 0.9, while the values of BFO and Bi–$C_3H_8O_3$ are from 0.6 to 1.0, which is characteristic of the mesoporous structure. The peak values of the pores of BFO and BFO–C_2H_5OH are concentrated at 14.5 and 7.0 nm, respectively. The mesopores of BFO are broader, while the mesopores of BFO–C_2H_5OH are more concentrated and the pore size distribution is more even [44] (Fig. 5(a) inset). From the inset in Fig. 5(b), peaks of Bi–$(CH_2OH)_2$ and Bi–$C_3H_8O_3$ PSD curves are centered at 12 and 3.5 nm, respectively, while the PSD of Bi–$C_3H_8O_3$ is more even than that of Bi–$(CH_2OH)_2$. The Brunauer–Emmett–Teller (BET) surface area, the pore volume and the average pore diameter of the sample were obtained by N_2 adsorption–desorption isotherms, and results are summarized in Table 2. It shows that BFO–C_2H_5OH has larger specific surface area (100.07 m^2/g) and smaller pore volume (0.195 cm^3/g) and average pore size (7.798 nm) than those of BFO, while Bi–$C_3H_8O_3$ has larger specific surface area (178.86 m^2/g) and smaller pore volume (0.216 cm^3/g) and average pore size (4.835 nm) than those of Bi–$(CH_2OH)_2$. The larger specific surface area can provide more reactive sites, thus adsorbing more dye molecules, which is more conducive to the photocatalytic reaction. In addition, a more uniform and ordered pore structure can enhance the periodicity of the material, and the contact area between the material and the dye molecules is larger, so that the photocatalytic activity is further improved [44]. This analysis was confirmed by results of the photocatalytic performance testing.

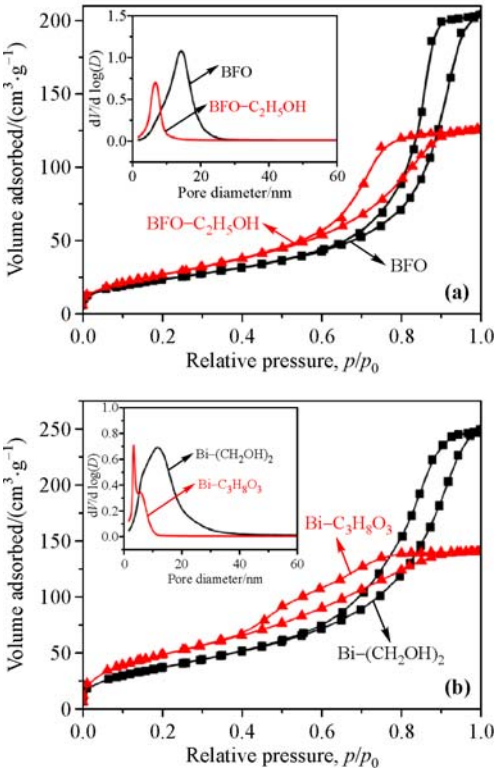

Fig. 5 Nitrogen adsorption–desorption isotherm plots and corresponding PSD curves (inset): **(a)** BFO and BFO–C_2H_5OH; **(b)** Bi–$(CH_2OH)_2$ and Bi–$C_3H_8O_3$.

Table 2 Structure parameters of different photocatalysts

Sample	$S_{BET}/(m^2 \cdot g^{-1})$	$V_{pore}/(cm^3 \cdot g^{-1})$	D_{pore}/nm
BFO	86.44	0.315	14.598
BFO–C_2H_5OH	100.07	0.195	7.798
Bi–$(CH_2OH)_2$	137.46	0.385	11.211
Bi–$C_3H_8O_3$	178.86	0.216	4.835

3.2 Optical properties

The optical properties of the samples were determined by UV-vis DRS and PL spectra. According to the Kubelka–Munk (K–M) theory, the experimentally measured UV-vis DRS spectra were converted to the corresponding absorption spectra, as shown in Fig. 6(a). It can be seen that the effective absorption wavelengths of BFO, BFO–C_2H_5OH, Bi–$(CH_2OH)_2$ and Bi–$C_3H_8O_3$ are different, and the cut-off wavelengths of both BFO and BFO–C_2H_5OH are in the visible range, which is basically consistent with the report in Refs. [24–45]. Bi–$(CH_2OH)_2$ and Bi–$C_3H_8O_3$ do not show obvious absorption edge. According to the XRD pattern, elemental bismuth could be synthesized using either ethylene glycol or glycerol as the solvent. The absorption peak (edge) of bismuth in the visible region is different and the photocatalytic mechanism of bismuth elemental has not yet reached a unified conclusion [13–16]. As a crystalline semiconductor, the optical absorption near the band edge follows the Tauc equation as follow:

$$(\alpha hv)^n = k(hv - E_g) \quad (2)$$

where α, hv, k and E_g are the absorption coefficient, the absorption energy, the absorption constant and the bandgap, respectively. The index n is equal to 2 for the direct transition and 1/2 for the indirect transition. Thus, E_g can be calculated by a plot of $(\alpha hv)^2$ versus hv as shown in Fig. 6(b). The estimated bandgap of BFO–C_2H_5OH is 1.90 eV, which is closer to reports in Refs. [18,46]. As a result, $Bi_{36}Fe_2O_{57}$ prepared using the ethanol solvent has a smaller bandgap and a high potential ability for visible-light response.

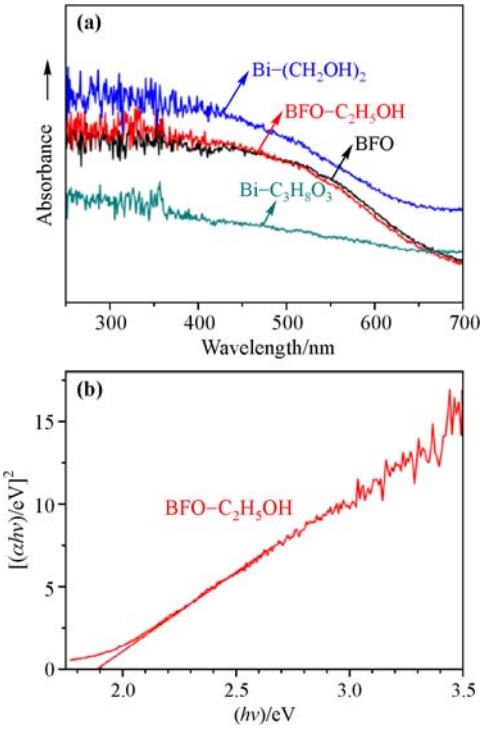

Fig. 6 **(a)** UV-vis DRS results of different catalysts and **(b)** the optical absorption edges.

The PL spectra of the samples are similar as all have broad peaks between 300 and 650 nm, especially for BFO, Bi–$(CH_2OH)_2$ and Bi–$C_3H_8O_3$. However, the PL spectrum of BFO–C_2H_5OH has some difference from others. As shown in Fig. 7, there is a convex peak between 323 and 375 nm. Compared with other three samples, the position of the main peak blue shifts to 323 nm and the luminescence intensity increases, which may be due to the lattice defects formed during the production, a defect level generated in the bandgap and indirectly light through surface defects [47–48]. From the spectra we can see that the position of the luminescence peak is constant, and the peak intensity becomes weaker in the order of Bi–$C_3H_8O_3$, BFO–C_2H_5OH, Bi–$(CH_2OH)_2$ and BFO in the visible region. Combined with SEM images, the change in peak intensity may be due to the presence of small particles on the surface of the crystal providing sites for electron–hole binding [49], resulting in the change of luminescence intensity, and the separation efficiency (δ) of photo-generated electron–hole pairs becomes larger in the order of δ(Bi–$C_3H_8O_3$) < δ(BFO–C_2H_5OH) < δ(Bi–$(CH_2OH)_2$) < δ(BFO). Material properties have effect on the photocatalytic performance [47]. According to the analysis of PL spectra, the optical property of BFO is better than that of BFO–C_2H_5OH. However, the photocatalytic activity of BFO–C_2H_5OH is higher than that of BFO, indicating that the optical property is merely one of the factors affecting the photocatalytic performance, but not the main one.

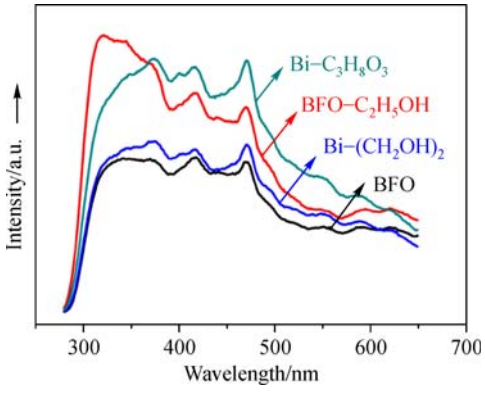

Fig. 7 PL spectra of different samples with the excitation wavelength of 260 nm.

3.3 Photocatalytic performance

The visible-light degradation of RhB was to evaluate the photocatalytic properties of different catalysts. As shown in Fig. 8(a), different photocatalysts have different degradation effects on the RhB solution with the same concentration. The degradation rate of RhB by P25 was only 2.8% after 60 min visible-light irradiation. BFO–C_2H_5OH displayed the best photocatalytic performance which degraded 23.2% of RhB after 60 min visible-light irradiation. Since the degradation equilibrium has not been reached yet at 60 min, the degradation rate will certainly increase if the photodegradation time is prolonged. The degradation rates of other samples after visible-light irradiation for 60 min were 9.3% (BFO), 10.2% (Bi–$(CH_2OH)_2$) and 16.4% (Bi–$C_3H_8O_3$). This result also

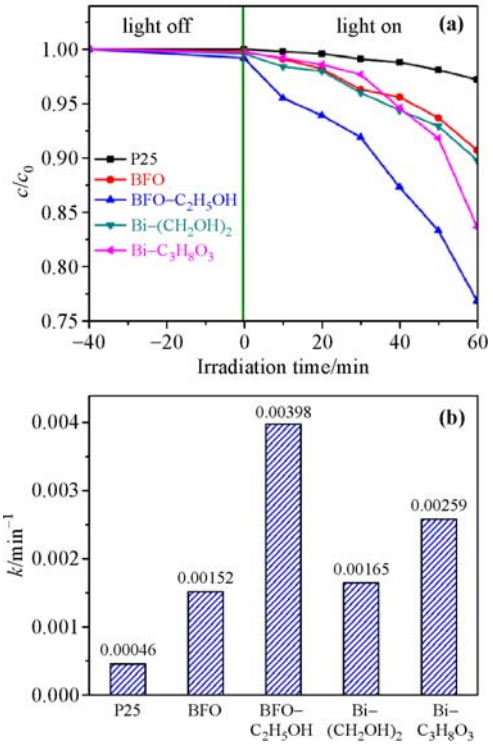

Fig. 8 **(a)** The reaction process and **(b)** the pseudo-first-order rate constant for the photocatalytic degradation of RhB with different catalysts.

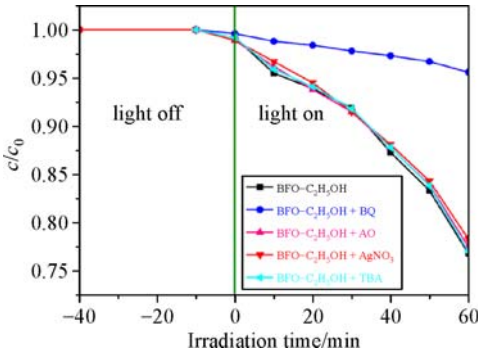

Fig. 9 Reaction process for the photocatalytic degradation of RhB on BFO–C_2H_5OH with and without trapping agents.

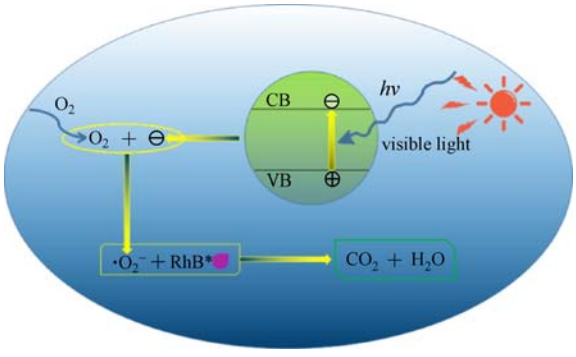

Fig. 10 The suggested mechanism diagram of the photocatalytic reaction.

corresponds to previous BET analysis of the materials. The kinetics of RhB degradation was studied by applying the pseudo-first-order model. The photodegradation rates of catalysts are 0.00046 min^{-1} (P25), 0.00152 min^{-1} (BFO), 0.00398 min^{-1} (BFO–C_2H_5OH), 0.00165 min^{-1} (Bi–$(CH_2OH)_2$) and 0.00259 min^{-1} (Bi–$C_3H_8O_3$) (Fig. 8(b)). The value of k for BFO–C_2H_5OH was 2.6 times higher than that of BFO, while 8.7 times higher than that of P25.

3.4 Photocatalytic mechanism

The reaction process for the photocatalytic degradation of RhB on BFO–C_2H_5OH is shown in Fig. 9. The degradation of RhB was significantly inhibited by the addition of BQ, indicating that superoxide radicals ($\bullet O_2^-$) play an important role among the four active substances produced by the photocatalytic reaction. However, the degradation rate was not significantly inhibited after adding other three capture agents such as AO, $AgNO_3$ and TBA. This suggests that photo-induced holes (h^+), electrons (e^-) and hydroxyl radicals (•OH) are not the most important active substances in the photocatalytic reaction.

Based on the above discussion, a plausible photocatalytic degradation mechanism as shown in Fig. 10 is suggested: (i) Dye molecules are firstly captured on the surface of the catalyst; (ii) The photocatalyst adsorbing RhB molecules is stimulated by visible-light irradiation, and the electronic migrate from the valence band to the conduction band, then the excited electron and the captured O_2 combined to form superoxide anion radical $\bullet O_2^-$; (iii) Superoxide radicals $\bullet O_2^-$ oxidize RhB molecules to CO_2 and H_2O, achieving the degradation of RhB.

4 Conclusions

In this work, a pure-phase sillenite-type photocatalyst $Bi_{36}Fe_2O_{57}$ and elemental bismuth was successfully prepared by the solvothermal method. The prepared samples were investigated by XRD, SEM, TEM, ICP, XPS, N_2 adsorption–desorption, UV-vis DRS and PL. The visible-light degradation of the RhB solution was employed to evaluate photocatalytic performance of the samples and BFO–C_2H_5OH was found to exhibit the best photocatalytic performance. Furthermore, the photocatalytic mechanism was discussed in depth, and the superoxide anion radical $\bullet O_2^-$ was regarded as the important active

material. This work provides a straightforward strategy for fabricating bismuth catalyst, holding promise for their application in the field of purifying polluted water resources.

Acknowledgements This project was supported by the Scientific Research Foundation for Young Scientists of Shanxi Province (201601D021134), the Scientific Research Foundation for Young Scientists of Taiyuan University of Science and Technology (20153008), the Start-up Fund for Doctorate Scientific Research Project of Taiyuan University of Science and Technology (20152017), and the Shanxi Provincial Student's Platform for Innovation and Entrepreneurship Training Program (2016282).

References

[1] Sharma S K, Sokhi S, Balomajumder C, et al. Reusable graphene oxide nanofibers for enhanced photocatalytic activity: a detailed mechanistic study. Journal of Materials Science, 2017, 52(9): 5390–5403

[2] Zhang X. Trend of and the governance system for water pollution in China. China Soft Science, 2014, (10): 11–24 (in Chinese)

[3] Zhang Z L, Sun X L. Present situation and development of dye wastewater treatment technology. Chemical Engineering Design Communications, 2017, 43(3): 205 (in Chinese)

[4] Sun A W, Chen H, Song C Y, et al. Preparation of magnetic $Bi_{25}FeO_{40}$–g-C_3N_4 catalyst and its high visible-light photocatalytic performance. Environmental Chemistry, 2013, 32(5): 748–754 (in Chinese)

[5] Xu P, Liu Y, Wei J, et al. Solvothermal preparation of Ag/TiO_2 nanoparticles and their photocatalytic activity. Acta Physico-Chimica Sinica, 2010, 26(8): 2261–2266 (in Chinese)

[6] Cong Y, Qin Y, Li X K, et al. Preparation and visible light photocatalytic activity of titanium dioxide coated multiwalled carbon nanotubes. Acta Physico-Chimica Sinica, 2011, 27(6): 1509–1515 (in Chinese)

[7] Ge L, Zhang X. Synthesis of novel visible light driven $BiVO_4$ photocatalysts via microemulsion process and its photocatalytic performance. Journal of Inorganic Materials, 2009, 24(3): 453–456 (in Chinese)

[8] Lin X, Lv P, Guan Q, et al. Bismuth titanate microspheres: Directed synthesis and their visible light photocatalytic activity. Applied Surface Science, 2012, 258(18): 7146–7153

[9] Nur'aeni, Chae A, Jo S, et al. Synthesis of β-FeOOH/Fe_3O_4 hybrid photocatalyst using catechol-quaternized poly(*N*-vinyl pyrrolidone) as a double-sided molecular tape. Journal of Materials Science, 2017, 52(14): 8493–8501

[10] Hu Z, Yuan L, Liu Z, et al. An elemental phosphorus photocatalyst with a record high hydrogen evolution efficiency. Angewandte Chemie International Edition, 2016, 55(33): 9580–9585

[11] Liu G, Niu P, Yin L, et al. α-Sulfur crystals as a visible-light-active photocatalyst. Journal of the American Chemical Society, 2012, 134(22): 9070–9073

[12] Liu G, Yin L C, Niu P, et al. Visible-light-responsive β-rhombohedral boron photocatalysts. Angewandte Chemie International Edition, 2013, 52(24): 6242–6245

[13] Qin F, Wang R, Li G, et al. Highly efficient photocatalytic reduction of Cr(VI) by bismuth hollow nanospheres. Catalysis Communications, 2013, 42: 14–19

[14] Ma D, Zhao J, Zhao Y, et al. An easy synthesis of 1D bismuth nanostructures in acidic solution and their photocatalytic degradation of rhodamine B. Chemical Engineering Journal, 2012, 209: 273–279

[15] Wang Z, Jiang C, Huang R, et al. Investigation of optical and photocatalytic properties of bismuth nanospheres prepared by a facile thermolysis method. The Journal of Physical Chemistry C, 2014, 118(2): 1155–1160

[16] Cui Z, Zhang Y, Li S, et al. Preparation and photocatalytic performance of Bi nanoparticles by microwave-assisted method using ascorbic acid as reducing agent. Catalysis Communications, 2015, 72: 97–100

[17] Wang Y, Chen J, Xu Q, et al. Novel visible-light-driven S-doped carbon dots/BiOI nanocomposites: improved photocatalytic activity and mechanism insight. Journal of Materials Science, 2017, 52(12): 7282–7293

[18] Wang K K, Wang X C, Xie H D. Synthesis and photocatalytic performance of a new photocatalyst $Bi_{36}Fe_2O_{57}$. Applied Chemical Industry, 2011, (12): 2084–2086, 2125 (in Chinese)

[19] Zhang C Y, Sun H J, Chen W, et al. Hydrothermal synthesis and photo-catalytic property of $Bi_{25}FeO_{40}$ powders. In: 2009 18th IEEE International Symposium on the Applications of Ferroelectrics. IEEE, 2009

[20] Ren L, Lu S Y, Fang J Z, et al. Enhanced degradation of organic pollutants using $Bi_{25}FeO_{40}$ microcrystals as an efficient reusable heterogeneous photo-Fenton like catalyst. Catalysis Today, 2017, 281: 656–661

[21] Yao W F, Wang H, Xu X H, et al. Sillenites materials as novel photocatalysts for methyl orange decomposition. Chemical Physics Letters, 2003, 377(5–6): 501–506

[22] Li B, Sun H J, Chen W, et al. Tunable hydrothermal synthesis of bismuth ferrites. Chinese Journal of Inorganic Chemistry, 2009, 25 (10): 1848–1852 (in Chinese)

[23] Hang Q, Zhu X, Zhu J, et al. Sillenite-type bismuth ferric nanocrystals: microwave hydrothermal synthesis, structural characterization, and visible-light photocatalytic properties. Procedia Engineering, 2012, 27: 616–624

[24] Xian T, Yang H, Dai J, et al. Preparation and photocatalytic performance of nano-bismuth ferrite with tunable size. Chinese Journal of Catalysis, 2011, 32(4): 618–623 (in Chinese)

[25] Ding L L, Jiang G J, Li W J, et al. Study on photocatalytic properties of $BiFeO_3$ prepared by hydrothermal method. Journal of Synthetic Crystals, 2013, 42(8): 1607–1615 (in Chinese)

[26] Wei X X, Cui H T, Guo S Q, et al. Hybrid BiOBr–TiO_2 nanocomposites with high visible light photocatalytic activity for water treatment. Journal of Hazardous Materials, 2013, 263(Pt 2): 650–658

[27] Wei X X, Chen C M, Guo S Q, et al. Advanced visible-light-driven photocatalyst BiOBr–TiO_2–graphene composite with graphene as a nano-filler. Journal of Materials Chemistry A: Materials for Energy and Sustainability, 2014, 2(13): 4667–4675

[28] He X H, Xiong M R, Ling Z Y, et al. Low-temperature sintering of NiCuZn ferrite for multilayer-chip inductor. Journal of Inorganic Materials, 1999, 14(1): 71–77 (in Chinese)

[29] Qin F, Li G, Xiao H, et al. Large-scale synthesis of bismuth hollow nanospheres for highly efficient Cr(VI) removal. Dalton Transactions, 2012, 41(37): 11263–11266

[30] Lin Y. Liquid Phase Synthesis and Characterization of Nanostructured Semiconductor Photocatalyst Bi–M–O (M = W, Fe). Dissertation for the Master Degree. Nanjing, China: Nanjing University of Science and Technology, 2012 (in Chinese)

[31] Zhao G Y, Tian Y, Fan H Y, et al. Properties and structures of Bi_2O_3–B_2O_3–TeO_2 glass. Journal of Materials Science and Technology, 2013, 29(3): 209–214

[32] Wang D, Li Y, Wang Q, et al. Nanostructured Fe_2O_3–graphene composite as a novel electrode material for supercapacitors. Journal of Solid State Electrochemistry, 2011, 16(6): 2095–2102

[33] Kothari D, Reddy V R, Gupta A, et al. Study of the effect of Mn doping on the $BiFeO_3$ system. Journal of Physics: Condensed Matter, 2007, 19(13): 136202

[34] Wandelt K. Photoemission studies of adsorbed oxygen and oxide layers. Surface Science Reports, 1982, 2(1): 1–121

[35] Wang Y P, Zhou L, Zhang M F, et al. Room-temperature saturated ferroelectric polarization in $BiFeO_3$ ceramics synthesized by rapid liquid phase sintering. Applied Physics Letters, 2004, 84(10): 1731–1733

[36] Ke H, Wang W, Wang Y, et al. Factors controlling pure-phase multiferroic $BiFeO_3$ powders synthesized by chemical co-precipitation. Journal of Alloys and Compounds, 2011, 509(5): 2192–2197

[37] Popa M, Crespo D, Calderon-Moreno J M, et al. Synthesis and structural characterization of single-phase $BiFeO_3$ powders from a polymeric precursor. Journal of the American Ceramic Society, 2007, 90(9): 2723–2727

[38] Xiao R, Yang R, Bian X, et al. PEG-assisted hydrothermal synthesis of $BiFeO_3$ powders and its photocatalytic property. Journal of Shaanxi Normal University (Natural Science Edition), 2013, 41(2): 39–43 (in Chinese)

[39] Liu Z D, Liang S, Li S Y, et al. Synthesis, microstructural characterization, and dielectric properties of $BiFeO_3$ microcrystals derived from molten salt method. Ceramics International, 2015, 41: S19–S25

[40] Zhang X J, Liu Y, Zhang Q, et al. Bismuth and bismuth composite photocatalysts. Progress in Chemistry, 2016, 28(10): 1560–1568 (in Chinese)

[41] Liu J L, Lai Q L, He L P, et al. Influence of preparing condition on characteristics and electronic property of nanometer-sized antimony tin oxide powders by hydrothermal method. Journal of Materials Science and Engineering, 2005, 23(4): 565–569 (in Chinese)

[42] He Y S, Li Z, Xi H X, et al. Research progress of gas–solid adsorption isotherms. Ion Exchange and Adsorption, 2004, 20(4): 376–384 (in Chinese)

[43] Kruk M, Jaroniec M. Characterization of modified mesoporous silicas using argon and nitrogen adsorption. Microporous and Mesoporous Materials, 2001, 44(SI): 725–732

[44] Wang Q, Shi Z C, Yang Y. Preparation and performance of titanium phosphate with different mesoporous structure. Chinese Journal of Power Sources, 2009, 33: 1064–1067 (in Chinese)

[45] Chen X Z, Qiu Z C, Zhou J P, et al. Large-scale growth and shape evolution of bismuth ferrite particles with a hydrothermal method. Materials Chemistry and Physics, 2011, 126(3): 560–567

[46] Zhang C Y. Hydrothermal Synthesis and Photics Properties Research of $Bi_{25}FeO_{40}$ Powders. Dissertation for the Master Degree. Wuhan, China: Wuhan University of Technology, 2010 (in Chinese)

[47] Yu C L, Yang K, Yu J C, et al. Hydrothermal synthesis and photocatalytic performance of Bi_2WO_6/ZnO heterojunction photocatalysts. Journal of Inorganic Materials, 2011, 26(11): 1157–1163 (in Chinese)

[48] Zheng L R, Huang B B, Wei J Y, et al. Optical properties of amorphous SiO_x:C particles calcined in air at elevated temperature. Acta Physica Sinica, 2012, 61(21): 217803 (7 pages) (in Chinese)

[49] Shi J Y, Chen T, Zhou G H, et al. Photoluminescence spectroscopy of $NaTaO_3$ and $NaTaO_3$:Bi^{3+} photocatalysts. Chemical Journal of Chinese Universities, 2007, 28(4): 692–695 (in Chinese)